Asymmetrical superelastic behavior of thermomechanically processed semi-equiatomic NiTi alloy in tensile and compressive modes of deformation

Asymmetrical Superelastic Behavior of Thermomechanically Processed Semi-equiatomic NiTi Alloy in Tensile and Compressive Modes of Deformation

A. Safdel[a], A. Zarei-Hanzaki[b,*], H. R. Abedi[c,*], S. Pourbabak[d], D. Schryvers[d], R.Basu[e]

[a] *Department of Mechanical Engineering, McMaster University, 1280 Main Street West, Hamilton, ON L8S 4L7, Canada*

[b] *Hot Deformation & Thermomechanical Processing Laboratory of High Performance Engineering Materials, School of Metallurgy and Materials Engineering, College of Engineering, University of Tehran, Tehran, Iran*

[c] *School of Metallurgy & Materials Engineering, Iran University of Science and Technology (IUST), Tehran, Iran*

[d] *Electron Microscopy for Materials Science (EMAT), University of Antwerp, Groenenborgerlaan 171, B-2020 Antwerp, Belgium*

[e] *School of Metal Construction Skills, Bhartiya Skill Development University (BSDU), Jaipur 302042, Rajasthan, India*

Abstract

In the present work two different cold working and annealing schemes were utilized, and the asymmetric superelastic response of thermomechanically processed materials were then assessed through cyclic tensile and compressive modes of deformation. The values of transformation stress, transformation strain, and pseudoelastic strain were measured for each treated and solutionized specimens and the asymmetric response was compared. In the solution annealed state, the difference of these parameters at different deformation modes was negligible due to the weak texture of the material, while for thermomechanically treated ones, development of specific deformation and recrystallization texture components was identified to be one of the underlying reasons of intensified asymmetry. The evolved substructure during the thermomechanical processing also played a substantial role in determining the asymmetric response. The presence of fine grains and dense dislocation substructure could hinder the movement of the transformation front, thus limiting the range of transformation. In tensile mode, the transformation stress was lower, but higher transformation strain was achieved, which was discussed relying on the slip activity in specified oriented grains. The lower transformation strain in compression mode led to lower pseudoelastic strain due to the narrow transformation range which finally degraded superelastic response of the material.

Keywords: NiTi; Superelasticity; Asymmetry; Texture; Thermomechanical processing; Recrystallization

* Corresponding authors
E-mail address: zareih@ut.ac.ir (Abbas Zarei-Hanzaki)
E-mail address: habedi@iust.ac.ir (Hamid Reza Abedi)

1. Introduction

Semi equiatomic NiTi alloys has attracted extensive attention owing to their unique functional properties; shape memory effect (SME) and superelasticity (SE) [1–3]. These properties along with fatigue resistance [4,5], high ductility [6,7] and acceptable biocompatibility [8,9], has led to the vast applications of this material, mainly in biomedical industry to produce stents, scaffolds, orthodontic wire, etc. [10–13].

Superelasticity (or pseudoelasticity) is attributed to the ability of the deformed material to recover high portions of strain during unloading at a certain temperature (above A_s), therefore creating a hysteresis loop in the stress-strain curve [14–16]. In NiTi alloys, this behavior is caused by the occurrence of the stress induced martensitic (SIM) transformation from the austenite parent phase, characterized by a stress plateau during loading, and reverse transformation from martensite to austenite during unloading [17–19]. The magnitude of the recoverable strain is reported to be lower than 8% and varies in each treating procedure [20–24].

Several studies have indicated the dissimilarity of stress-strain curves of superelastic NiTi in different modes of deformation, such as uniaxial tension, uniaxial compression, torsion, and compression shear [25–29]. This so-called asymmetric behavior denotes the different responses of the material to each deformation mode and is believed to be directly correlated with thermos-elastic martensitic transformation, in which a highly symmetrical austenitic structure (cubic B2) transforms into the lower symmetry martensitic (monoclinic B19') phase [25]. Fig. 1 demonstrates the asymmetrical behavior of NiTi alloys, during a load-unloading cycle in tensile and compressive modes of deformation. Several important parameters, namely transformation strain, SIM transformation stress, width of the stress hysteresis, and slope of the transformation region that are normally utilized to quantitatively define the asymmetric properties and are shown on the graph.

As is apparent, a clear difference exists between these parameters, emphasizing the asymmetrical behavior of the material. The measurement strategy for each parameter and explanation of the deformation mechanisms of the material will be discussed later in the paper.

The asymmetry behavior of NiTi alloys is a matter of great importance, which should be carefully considered in designing engineering components which experience multiple modes of deformations during application. Despite this significant impact, the asymmetric response of post-treated NiTi alloys has been rarely addressed, and yet still, not fully comprehended. However, few attempts have been conducted to examine this phenomenon in different deformation modes, through qualitative, quantitative or modelling approaches [30–32].

Primarily, it was believed that texture-free NiTi alloys exhibit no tension-compression asymmetry, and the formation of preferential texture components is the only underlying reason behind the observed differences in the behavior of the alloy in tensile and compressive modes of deformation. It was then concluded that orientations near <111> along the loading direction are favored in tension, while orientation along <100> are preferred in compression [12,30,32–34]. However, later studies rejected the previous assumptions, proving that asymmetry can also be observed during the deformation of NiTi alloys that possess grains with random orientations. Šittner et al. [35] performed a systematic study in which it was revealed that NiTi alloys with randomly oriented grains exhibit asymmetry in view of transformation strain, transformation stress, the width of stress hysteresis and other characteristics of the stress-strain superelasticity curves. Furthermore, Stebner et al. [36,37] stated the imperative role of the changes in the crystal structure of the material during the $B2 \rightarrow B19'$ transformation on the asymmetrical response of the material. It was well established that the low-symmetry monoclinic martensitic phase can result in a various number of twinning modes, which govern the tension-compression asymmetry of the

material and determine the differences in the strains and driving forces in each of the deformation modes. Martensite slip and hardening effects in compression were found to be highly probable, where fewer twinning systems are activated. Therefore, in contrast to previous beliefs, asymmetry was introduced as an inherent property of NiTi alloys and the load dependency of the martensitic transformation, proving that even randomly oriented exhibit an asymmetrical response. However, the intertwined nature of the asymmetric behavior and the martensitic transformation has led to numerous challenges in fully understanding the deformation behavior of NiTi alloys and is a topic truthfully worth investigating. Although the asymmetric response in NiTi alloys with random texture was confirmed, the evolved texture of the material during the processing stage can still affect the asymmetry parameters. For instance, Mao et al. [38,39] quantitatively correlated the texture and asymmetry, in a solution annealed Ni50.8%-Ti alloy, by exploiting the high-end in-situ electron backscattered diffraction (EBSD) technique. They established that the stress levels at which the SIM transformation occurs is highly dependent to the texture of the material.

Coming to the point, most of the previous involved research were utilizing single crystals or solution annealed polycrystals, which commonly exhibit inferior superelastic properties. The low value of the critical resolved shear stress (CRSS) of these specified microstructures, hinders the occurrence of the SIM transformation, and triggers the activation of slip systems [40,41]. However, if an appropriate thermomechanical processing route is implemented, the superelastic behavior of the material will be significantly improved. Accordingly, the differences in most important asymmetry parameters (i.e. critical stress and strain of SIM, and pseudoelastic strain) under the various deformation modes, is expected to be intensified in the case of thermomechanically processed materials. In this respect, in the present research the asymmetric behavior of two different cold worked and annealed specimens, which are dominantly used in most

engineering applications, will be scrutinized and compared to solution annealed state. This will provide a proper condition to assess the correlation of superelastic behavior and asymmetric response of the material. The authors believe that the texture cannot be considered as the only governing factor, and the occurrence of restoration processes and substructure development is also expected to be imperative.

2. Experimental procedures

A 50.5Ni-49.5Ti (at. %) alloy was homogenized at 1000ºC for 3 hours and then rolled to 64% of thickness reduction at 1000ºC. Solution treatment was then performed at 850ºC for 2 hours in a furnace equipped with high purity argon gas to reduce the effect of oxidization and the samples were subsequently quenched in room temperature water. Fig. 2(a) demonstrates the X-ray diffraction (XRD) pattern of the solution annealed sample, confirming the existence of only the austenite parent phase in the microstructure, and Fig. 2(b) represents the grain size distribution of the solution annealed material, which was obtained by EBSD, showing an average grain size of 65μm $\pm$ 3 μm.

The superelastic behavior of the solution annealed material (labeled as SA) and the thermo-mechanically processed specimens were examined under both tensile and compressive modes of deformations. A wide range of cold working and annealing conditions was utilized to process the samples in which two true strain values of 0.2 and 0.5 were utilized for the initial cold compression. Subsequent annealing was performed at 400 and 500°C for the duration of 10, 30, 60, and 120min. Samples were quenched in room-temperature water after conducting the mentioned heat-treating procedures. A detailed view of the tensile superelastic behavior of each processed sample has been identified in [14]. Nonetheless, the summary of that work along with the sample labels, processing condition and superelasticity properties, are presented in Table 1. Accordingly,

superelastic response of the samples were compared considering the critical value of SIM stress and the residual strain after unloading. It was found out that the sample which was cold compressed to true stain of 0.2 and annealed at 400ºC for 120 min (CC-0.2-400-120) along with another sample which was compressed to true strain of 0.5 and heat treated at the same temperature for 60 min (CC-0.5-400-60) demonstrated enhanced superelasticity and the lowest residual strain values – 2.6% and 2.1% respectively. Therefore, in the present work, those two samples were selected for further investigation of the tension-compression asymmetry.

Cold compression was conducted utilizing a GOTECH AI-7000 universal testing machine in accordance with ASTM-E9 standard [42] at room temperature under the strain rate of $0.001s^{-1}$, and the subsequent heat treatment was carried out in a tube furnace using a protective argon atmosphere. Annealed samples were promptly quenched in water at room temperature after the heat treatment procedure.

In order to investigate the superelastic response of the material in tensile and compressive modes, specimens were prepared in accordance with ASTM-E8 [43] and ASTM-E9 for tension and compression test, respectively, and keeping the aspect ratio of the standards. Both tension and compression specimens were cut from the middle part of the primarily compressed specimens using an electro-discharge machine (EDM). The superelastic response was examined after loading up a specimen to 11% engineering strain and then unloading back to the initial state, using a SANTAM STM-50 universal testing machine with the crosshead speed of 0.1 $mm.m^{-1}$. To maintain consistency and assure the results, each test was carried out three times for each processed sample.

An FEI Quanta-3D field emission gun (FEG) scanning electron microscope (SEM) operating at an acceleration voltage of 20 kV equipped with an EBSD system from EDAX-TSL

was utilized to examine the microstructural evolution in all samples. Samples were electropolished at 0°C and 18 V in an electrolyte of methanol with 10% perchloric acid to obtain a strain free surface for better pattern acquisition. Transmission electron microscopy (TEM) images and selected area electron diffraction (SAED) patterns were acquired using an FEI Tecnai G2 instrument operating at 200 kV to better reveal the substructural features of the treated samples. For TEM sample preparation, discs of 3 mm diameter were cut from all the samples using an electro-spark erosion machine, followed by grinding down to ~120 μm thickness. These discs were further electropolished with a mixture of 80% methanol and 20% sulfuric acid at -5 °C employing a Struers Tenupol twinjet electropolishing equipment for thinning down the edges of the perforated sample for TEM investigations.

3. Results and Discussion

3.1. Asymmetric superelastic behavior in different modes of deformation

A schematic representation of the load-unloading curves in superelasticity assessment during tension and compression was illustrated in Fig. 1. According to the behavior of the alloy during tension, the deformation mechanism is divided into three different zones, as is pointed out in the figure. Accordingly, in zone I, austenite phase experiences an elastic deformation until reaching a certain level of stress, which is known as the required stress for the occurrence of SIM transformation (σ_{SIM}). The value of this parameter is extracted by the intersection of two tangent lines which are plotted along the elastic line and the plateau of the transformation. Zone II reveals the transformation region, in which different martensite variants are mechanically induced during deformation. The strain range of the SIM transformation is shown on the graph, which will be utilized in the following sections to quantitatively compare the superelasticity and asymmetry. In zone III, two main deformation modes are involved: (1) dislocation movement and activation of

slip systems in austenite and (2) further progress of the SIM transformation in the residual parent phase. Further loading primarily leads to the elastic deformation of martensite phase, and ultimately, the activation of slip systems in this phase (not plotted in the graph) [36,44,45]. The pseudoelastic strain is another factor which is of utmost importance since it indicated the reversibility and the degree of superelasticity. As was plotted in Fig. 1, this parameter is obtained from the deviation of the unloading section of the curve from the straight unloading line.

Fig. 3(a) demonstrates the loading-unloading curves of SA in both tensile and compressive modes of deformation. As is evident, the response of the material is different in each mode, indicating an asymmetrical response. The three mentioned parameters, namely SIM stress, pseudoelastic strain, and transformation strain, were utilized for quantitative comparisons and their values were extracted from both curves, which are represented in Fig. 3(b). Although the measured values are nearly the same for each mode, the required stress to trigger the transformation of austenite to martensite is higher in compression and both transformation and pseudoelastic strain possess higher values in tension. Prior to discussing the underlying reasons of these findings, loading-unloading curves of thermomechanically processed samples are represented in Fig. 4. At a glance, a strong asymmetrical response is apparent when thermomechanically processed specimens are compared to SA. The values of asymmetry parameters for CC-0.2-400-120 and CC-0.5-400-60 are shown in Fig. 4(c) and Fig. 4(d), respectively. For each processed specimen, when compressive curve is compared to tensile curve, a higher value of transformation stress, a lower value of pseudoelastic strain, and a lower value of transformation strain is observed. Furthermore, a comparison between CC-0.5-400-60 and CC-0.2-400-120, SIM stress was found to be higher in the former sample, while pseudoelastic strain and transformation strain are lower. This difference is especially pronounced in the compressive mode. In the following the microstructure of the

sampled prior to the tension and compression load-unload tests will be investigated and the results will be correlated to texture and microstructure evolution of each specimen.

3.2. Microstructural characterization prior to tension-compression tests

The texture of the solution annealed material is illustrated in the Fig. 5(a) through correlated inverse pole figure (IPF) of the B2 austenite phase. The intensity of texture for this sample (maximum value of 2.2) was found to be very low, which is due to the solution annealing treatment. Nonetheless, the sample was previously hot rolled, thus traces of a minor favorable reorientation of grains toward the <111> direction in a direction parallel to the loading direction is still quite apparent. Fig. 5(b) exhibits the misorientation angle distribution of the low and high angle grain boundaries in the solution annealed specimen, and as is noticeable, the majority of the boundaries have a misorientation angle of higher than 15º, which proves that most boundaries are high angle grain boundaries (HAGB). On the other hand, only a low fraction of low angle grain boundaries (LAGB) is present in the microstructure, which confirms that no significant substructure has been formed during the treating process.

In the case of thermomechanically processed specimens, since they were subsequently annealed after enduring a high level of compressive stresses, restoration mechanisms are indeed expected to occur, thereby interfering with the texture and microstructure of the material. Fig. 6, illustrates the IPFs acquired from EBSD scans of the cold compressed and subsequently annealed specimens. As is shown in Fig. 6(a), CC-0.2-400-120 specimen has been highly texturized, and the value of texture intensity is found to be higher than 6. The extremely large portions of the grains, and therefore each scanned point in the microstructure are aligned toward the <111> direction, which is parallel to the normal direction of the compressive deformation. Several studies mentioned similar results indicating that in a BCC material, grains tend to orient along <111>

direction during cold rolling or compression. Additionally, it was previously mentioned that the solution annealed material, had a weak <111> texture due to the applied rolling stage. Hence, by applying higher compressive loads, the preexisted texture is significantly intensified specifically in the <111> direction. Fig. 6(b), on the other hand, shows the IPF of CC-0.5-400-60 specimen, in which a dramatic drop in texture intensity is evident in comparison with CC-0.2-400-120. This variation points to the fact that the amount of reduction in cold compression can govern the texture of the material, mainly by determining the dominant restoration mechanism. Accordingly, by increasing the reduction for CC-0.5-400-60, the driving force for the occurrence of static recrystallization is increased and therefore recrystallization is stimulated and acts as the main restoration mechanism instead of static recovery. Since static recrystallization introduces its own unique texture components throughout the microstructure, the intensity of texture is significantly increased in <321> direction. In other words, the intensity of the preferential texture along the <111> direction (deformation texture) is decreased, due to the rapid development of another texture component along <321> direction (recrystallization texture).

TEM images and SAED patterns were utilized to further confirm these statements, and also identify the substructural development of the processed materials during the performed cold compression and annealing treatment. For CC-0.2-400-120, these images are demonstrated in Fig. 7. The existence of austenite bands is clearly apparent in Fig. 7(a), which is displayed by colored dashed lines. Initial studies suggested that these bands are traces of the residual martensite plates which were formed during cold working and then reverted to austenite in the subsequent heating stage. This confusion was fully addressed by Molnárová et al. [46], who indicated that those residual martensite plates cannot be observed in the microstructure since they do not leave any lattice defects. Instead, these are traces of deformation bands which were created by further

distortion of the B19′ martensite phase during the cold working process. Although during heating, martensite transforms back to austenite, those permanent lattice defects and the observed austenite bands are apparent in the microstructure. Higher magnification TEM image of this area is presented in Fig. 7(b), which indicates that these parallel plates are split into smaller subgrains. The corresponding SAED pattern from the circled area in Fig. 7(b) is demonstrated in Fig. 7(c), revealing the presence of B2 austenite phase. Since the SAED pattern was acquired from an area encompassing a few neighboring subgrains with small deviations between their orientations, some spots are elongated in the diffraction pattern. The existence of subgrains and the low misorientation angle between them points to the fact that static recovery was the dominant restoration mechanism during annealing of CC-0.2-400-120. Nonetheless, there are a few other weak spots, which are believed to be an indication of another phase. For further investigation, other areas of the sample were scrutinized. The formation of Ni_4Ti_3 lenticular precipitates was confirmed by Fig. 7(d). The presence of these finely dispersed precipitates not only increases the CRSS, but also depletes the matrix from nickel. Therefore, Ni_4Ti_3 precipitates, on the one hand, strengthen the matrix and improve the cyclic stability of the material, and on the other hand, increase the transformation temperatures, leading to lower transformation stresses and enhanced superelastic properties. Due to that, this sample is expected to show an enhanced superelastic response in comparison to the annealed sample. Fig. 7(e) illustrates a higher magnification image of the same area, and the yellow circle indicates the region which was utilized to acquire the SAED patterns that are shown in Fig. 7(f). The corresponding pattern proves the presence of R-phase, which is an intermediate trigonal phase. R-phase could be formed during the reversion of B19’ martensitic plates to B2 austenitic phase in areas near the precipitates, when a Ni-rich NiTi alloy is aged after cold working [47,48]. Although the sample is heat treated after cold compression, in very few areas within the grains, as

is depicted in Fig. 7(g), B19' martensitic variants were found. The presence of martensite twins in some areas of a cold worked and annealed sample can be attributed to two main factors, (1) inhomogeneous formation of Ni_4Ti_3 precipitates, which depletes the matrix from nickel, and results in increasing the onset temperature of the martensitic transformation, and (2) the lattice distortion and increase in the dislocation density during cold working stage, which promotes the formation of (001) compound twins and their perseverance even after the conducted heat treatment. SAED pattern (Fig. 7i) from the area depicted in Fig. 7(h) revealed that the observed martensite twins in that zone are indeed (001) compound twins [49]. Martensite stabilization and the presence of martensite phase after cold working and annealing was also reported by other investigations [50–53].

Fig. 8(a) illustrates the TEM images of CC-0.5-400-60, confirming the presence of subgrains, which are less plate-like, along with a partially recrystallized finer structure. Static recrystallization plays a prominent role in defining the microstructure of a material which may occur when a cold worked material is subsequently annealed at elevated temperatures. During cold compression, the free energy of the material is increased by the presence of dislocations across the sample, resulting in a thermodynamically unstable structure. For materials deformed to a critical level of strain (e. g. CC-0.5-400-60), static recrystallization during the annealing stage is expected to occur, causing the gradual migration of dense dislocation networks and subgrains, and resulting in the formation of high angle grain boundaries, fresh grains, and a more stable low-density structure. The occurrence of static recrystallization was also reported by other studies for cold worked and annealed NiTi specimens [54–57]. Higher magnification TEM image and the corresponding SAED pattern from the indicated circled area are shown in Fig. 8(b) and Fig. 8(c), respectively. Indexing the SAED patterns in Fig. 8(c) revealed that B2 austenitic phase results in

the best fitting. It is worth mentioning that the SAED pattern was acquired from a very small area comprising of a few neighboring grains, which were slightly misoriented relevant to each other. Thus, the pattern resembles a single crystal, while in fact the material is polycrystalline. The presence of martensite was also revealed by examining some areas of the sample, as is illustrated in Fig. 8(d), and the corresponding pattern from the circled region in Fig. 8(e), identified them as (001) compound twins and also revealed the presence of B2 austenite phase, as is depicted in Fig. 8(f). The underlying reasons behind the existence of martensite twins was discussed earlier in the paper. The observed TEM images from CC-0.5-400-60 reveals that static recrystallization undoubtedly played a major role in defining the microstructure of this sample.

Thus far, it has been concluded that CC-0.2-400-120 experienced static recovery as the dominant restoration mechanism, while static recrystallization was of higher impact to the microstructure of CC-0.5-400-60. For better clarification, EBSD data and grain boundary misorientation angles were utilized to plot the fractions of LAGBs and HAGBs in each sample, and the result is demonstrated in Fig. 9. In this figure, CC-0.2-400-120 possesses a higher share of LAGBs compared to CC-0.5-400-60 and therefore lower HAGBs. Higher LAGB signifies the presence of a strong substructure and subgrain formations for the compressed specimen to true strain of 0.2, which points out the dominancy of static recovery. However, for the compressed specimen to true strain of 0.5, a considerably lower amount of subgrains is apparent, which supports the fact that new grains were formed because of static recrystallization. However, more than 10% of the boundaries in CC-0.5-400-60 were identified to be LAGB, so recrystallization could occur just partially.

3.3. The relationship between asymmetric parameters and texture

Fig. 10 represents the EBSD grain orientation distribution along the loading direction of the tensile and compressive loading-unloading tests for each specimen in a unique IPF triangle. The black dots in each triangle correspond to the crystallographic orientation of each scanned spot on the sample. This figure is particularly important since it can be utilized to describe the differences in the deformation behavior of the samples in each mode of deformation.

Twinning systems in NiTi alloys are typically classified into three different types (type I, type II, and compound twinning modes). Type II twinning is believed to play the dominant role during the deformation of superelastic NiTi alloys [58], which led the authors to mainly assume the activity of this system. TEM observations and crystallographic relationships introduced the $\{\overline{0.86840}\ 0.2688\ 0.4138\} < 0.4580\ 0.7706\ 0.4432 >$ shearing system to create the optimum shearing angle for the type II twinning mode [38,58,59]. Mao et al. [38,39], implemented the aforementioned shearing system to calculate the Schmid factors (SF) of 100 different crystallographic orientations, as is shown in Fig. 11(a). This figure will be used to justify the findings of this paper since it shows a comparison between tension and compression SFs in each crystallographic direction (loading direction). It is worth mentioning that martensite variant selection during the SIM transformation is theoretically governed by the Schmid's law. Although the deformation mechanism is the same during tension and compression, the value of the critical resolved shear stress (CRSS) and the maximum resolved shearing factor (MSRF) for the formation of each martensite corresponding variant pairs (CVPs) is different. As a result, tensile and compressive SFs, which are proportional to the CRSS in each mode are different as well [30,38]. Clearly, the higher value of the SF for a specific orientation indicates that the shearing system is more probable to be activated. Furthermore, Mao et al. [39] and Sittner et al. [35], calculated the

lattice distortion caused by the $B2 \rightarrow B19'$ transformation and measured the transformation strain for different crystallographic orientation in an IPF, for each lattice correspondence martensite variants in both tensile and compressive modes of deformation. From a thermodynamic perspective, the martensite variant that can provide the highest strain in a direction along the applied load is stimulated to form since it generates the highest driving force for the SIM transformation. Fig. 11(b), shows the comparison of transformation strains in each crystallographic direction for both tensile and compressive modes of deformation [38].

SF and transformation strain calculations with respect to the crystallographic directions, point out the relative importance of texture in the response of the material to each mode of deformation. To this end and for better interpretation of the measured value of asymmetry parameters, the achieved orientation distribution for each sample (Fig. 10) was superimposed to Fig. 11, and the results are represented in Fig. 12.

It was explained that SA was only slightly texturized and as is shown in Fig. 12(a) the black spots in the orientation distribution are not accumulated in one specific zone and are scattered throughout the IPF triangle. According to Fig. 3, SA also showed a slight difference in asymmetry parameters during compressive and tensile modes of deformation. Higher transformation stress in compression was recorded, which can be justified by the higher density of the black dots in the red zone (higher SF in tension) of Fig. 12(a-1). Higher Schmid factor denotes that lower applied stress is needed to activate the SIM transformation. Moreover, both transformation strain and pseudoelastic strain were found to be higher in tension in comparison with compression. Fig. 12(a-2) shows that for most orientations, most spots are in the red zone, which means that tensile transformation strain is higher. Pseudoelastic strain can be correlated to transformation stress i.e., the higher the transformation stress, the higher the induced martensite variants and the higher the

probability of reversion. This results in enhanced superelasticity and thereby higher pseudoelastic strain after unloading. Accordingly, for treated samples, as it was shown in Fig. 4(c,d), the achieved pseudoelastic strain is lower in compression since SIM transformation was limited to a narrow strain range. Fig. 12(b,c) represents the mentioned superimpositions for both treated specimens. In Fig. 12(b), the accumulation of black dots in orientations close to the [111] direction for CC-0.2-400-120 indicated a highly texturized structure, which was named deformation texture earlier in the paper. Therefore, as is depicted, the majority of diffraction spots are located in the red zone of the IPFs, which denotes higher values of both SF and transformation strain in tensile mode. Hence, lower stress is needed to initiate the SIM transformation in tension and also the amount of transformation strain and pseudoelastic strain are anticipated to be higher. This figure therefore justifies the measured asymmetry parameters Fig. 4(c).

For CC-0.5-400-60, according to Fig. 12(c), the low-intensity recrystallization texture is found to be evolved in orientations close to the red zones. On the one hand, the required SIM stress is expected to be higher in compression and on the other hand transformation strain and pseudoelastic strain should be higher in tension. Thus, the measured asymmetry parameters for CC-0.5-400-60 (Fig. 4d) are in complete agreement with the interpretation of this figure. Although the evolved texture could mostly address the asymmetrical behavior of the processed alloys and the underlying reason for the different values, other important aspects should also be considered, specifically when different samples are compared. These factors are addressed in the next section.

3.4 The relationship between asymmetric parameters and substructural evolutions

Besides texture, asymmetry parameters and SIM Transformation are believed to be affected by other microstructural features like substructure, dislocation state, subgrains, and preexisting martensite variants. Hence these characteristics should be investigated, especially

when different specimens are compared. As was demonstrated in Fig. 4(c,d), SIM stress was found to be higher in CC-0.5-400-60, compared to CC-0.2-400-120, in both deformation modes. This could be attributed to the effects of the initial cold working stage and the microstructural evolution in the subsequent heating process. On the one hand, CC-0.5-400-60 has a fine grained partially recrystallized structure, and on the other hand, higher reduction in cold compression resulted in higher density of dislocations. Both these features (recrystallized grains and dislocations) could act as barriers to the movement of martensitic transformation which hinders the occurrence of SIM transformation, thus higher level of stress is required for further continuation of the transformation. Furthermore, higher transformation strain and the pseudoelastic strain was recorded for CC-0.2-400-120, especially in compressive mode. This also could be due to the presence of finer grains and a denser dislocation structures in CC-0.5-400-60 since strain accommodation, and martensitic transformation is reported to be hindered in the presence of very fine grains, defects, and dense dislocation networks [60]. It was shown in Fig. 4(a,b) that the slope of the graphs in the compressive mode was significantly higher in the transformation zone, and at the same level of strain, higher stresses were obtained during compression. The higher the level of stress during the deformation and the slope of the curve, the higher the probability of surpassing CRSS and therefore the activation of slip systems. Therefore, the SIM transformation is further constrained, resulting in lower transformation strain and a deteriorated superelastic response for CC-0.5-400-60 in compression. Although the relationship between the asymmetric behavior of NiTi alloys and substructure was discussed in this section based on the author's understanding, more in-depth studies are still required to define the correlation between these two important features.

4. Conclusion

The asymmetric superelastic behavior of NiTi alloy, treated through cold work and annealing, was investigated in tension and compression modes of deformation. The high fraction of LAGBs and subgrains formation indicated that static recovery was the prevailing mechanism for CC-0.2-400-120, while the significantly higher frequency of HAGBs in CC-0.5-400-60 signified that this specimen mainly experienced static recrystallization. In the former specimen, a high intensity deformation texture was observed along the <111> direction parallel to the compression axis, and the recrystallized structure in the latter created a low intensity texture along <321> directions. The texture and evolved substructure were found to be highly influential with respect to the asymmetric behavior of the material. In all specimens, lower transformation stress, but higher transformation strain was recorded in tensile mode, which was attributed to the presence of grains which were oriented toward directions with higher Schmid factor. Higher transformation stress was also achieved for CC-0.5-400-60, compared to CC-0.2-400-120 in both modes, which was attributed to the presence of fine grains and dense dislocation substructure. These features could hinder the movement of the transformation front, thus limiting the range of transformation. In compression, significantly lower transformation strains and degraded superelastic response was attributed to the facilitated activation of slip systems. Lower transformation strain could lead to Lower pseudoelastic strain due to the narrow transformation range.

Data Availability

The raw/processed data required to reproduce these findings cannot be shared at this time as the data also forms part of an ongoing study.

References

[1] S.W. Robertson, a R. Pelton, R.O. Ritchie, Mechanical fatigue and fracture of Nitinol, Int. Mater. Rev. 57 (2012) 1–37. doi:10.1179/1743280411Y.0000000009.

[2] K. Otsuka, X. Ren, Physical metallurgy of Ti-Ni-based shape memory alloys, Prog. Mater. Sci. 50 (2005) 511–678. doi:10.1016/j.pmatsci.2004.10.001.

[3] E. Patoor, D.C. Lagoudas, P.B. Entchev, L.C. Brinson, X. Gao, Shape memory alloys, Part I: General properties and modeling of single crystals, Mech. Mater. 38 (2006) 391–429. doi:10.1016/j.mechmat.2005.05.027.

[4] A.R. Pelton, V. Schroeder, M.R. Mitchell, X.Y. Gong, M. Barney, S.W. Robertson, Fatigue and durability of Nitinol stents, J. Mech. Behav. Biomed. Mater. 1 (2008) 153–164. doi:10.1016/j.jmbbm.2007.08.001.

[5] H. Yin, Y. He, Z. Moumni, Q. Sun, Effects of Grain size on tensile fatigue life of nanostructured NiTi shape memory alloy, Int. J. Fatigue. 88 (2016) 166–177. doi:10.1016/j.ijfatigue.2016.03.023.

[6] G.S. Firstov, J. Van Humbeeck, Y.N. Koval, High-temperature shape memory alloys Some recent developments, Mater. Sci. Eng. A. 378 (2004) 2–10. doi:10.1016/j.msea.2003.10.324.

[7] M. Mahmoudi, I. Karaman, J. Ma, G. Tapia, B. Franco, A. Elwany, R. Arroyave, On the printability and transformation behavior of nickel-titanium shape memory alloys fabricated using laser powder-bed fusion additive manufacturing, J. Manuf. Process. 35 (2018) 672–680. doi:10.1016/j.jmapro.2018.08.037.

[8] M. Es-Souni, M. Es-Souni, H. Fischer-Brandies, Assessing the biocompatibility of NiTi shape memory alloys used for medical applications, Anal. Bioanal. Chem. 381 (2005) 557–567. doi:10.1007/s00216-004-2888-3.

[9] M. Ataei, A. Zarei-Hanzaki, A. Shamsolhodaei, Shape memory response and mechanical properties of warm deformed NiTi intermetallic alloy, Mater. Sci. Eng. A. 680 (2017) 291–296. doi:10.1016/j.msea.2016.10.104.

[10] J.W. Mwangi, L.T. Nguyen, V.D. Bui, T. Berger, H. Zeidler, A. Schubert, Nitinol manufacturing and micromachining: A review of processes and their suitability in processing medical-grade nitinol, J. Manuf. Process. 38 (2019) 355–369. doi:10.1016/j.jmapro.2019.01.003.

[11] M. Speirs, B. Van Hooreweder, J. Van Humbeeck, J.P. Kruth, Fatigue behaviour of NiTi shape memory alloy scaffolds produced by SLM, a unit cell design comparison, J. Mech. Behav. Biomed. Mater. 70 (2017) 53–59. doi:10.1016/j.jmbbm.2017.01.016.

[12] K. Gall, H. Sehitoglu, Role of texture in tension-compression asymmetry in polycrystalline NiTi, Int. J. Plast. 15 (1999) 69–92. doi:10.1016/S0749-6419(98)00060-6.

[13] C. Bourauel, W. Scharold, a. Jäger, T. Eliades, Fatigue failure of as-received and retrieved NiTi orthodontic archwires, Dent. Mater. 24 (2008) 1095–1101. doi:10.1016/j.dental.2007.12.007.

[14] A. Safdel, A. Zarei-Hanzaki, A. Shamsolhodaei, P. Krooß, T. Niendorf, Room temperature superelastic responses of NiTi alloy treated by two distinct thermomechanical processing schemes, Mater. Sci. Eng. A. 684 (2017) 303–311. doi:10.1016/j.msea.2016.12.047.

[15] H. Shahmir, M. Nili-Ahmadabadi, F. Naghdi, M. Habibi-Parsa, I. Haririan, Control of Superelastic Behavior of NiTi Wires Aided by Thermomechanical Treatment with Reference to Three-Point Bending, J. Mater. Eng. Perform. 23 (2014) 1386–1391. doi:10.1007/s11665-014-0901-3.

[16] B. Kockar, I. Karaman, J.I. Kim, Y.I. Chumlyakov, J. Sharp, C.J. (Mike) Yu, Thermomechanical cyclic response of an ultrafine-grained NiTi shape memory alloy, Acta Mater. 56 (2008) 3630–3646. doi:10.1016/j.actamat.2008.04.001.

[17] Y. Liu, The superelastic anisotropy in a NiTi shape memory alloy thin sheet, Acta Mater. 95 (2015) 411–427. doi:10.1016/j.actamat.2015.03.022.

[18] X. Huang, Y. Liu, Effect of annealing on the transformation behavior and superelasticity of NiTi shape memory alloy, Scr. Mater. 45 (2001) 153–160. doi:10.1016/S1359-6462(01)01005-3.

[19] H. Sehitoglu, J. Jun, X. Zhang, I. Karaman, Y. Chumlyakov, H.J. Maier, K. Gall, Shape memory and pseudoelastic behavior of 51.5%Ni-Ti single crystals in solutionized and overaged state, Acta Mater. 49 (2001) 3609–3620. doi:10.1016/S1359-6454(01)00216-6.

[20] N. Resnina, S. Belyaev, A. Shelyakov, V. Rubanik, V. Rubanik, R. Konopleva, V. Chekanov, E. Ubyivovk, M. Krzhizhanovskaya, Pre-martensitic phenomena in Ti40.7Hf9.5Ni44.8Cu5 shape memory alloy, Intermetallics. 67 (2015) 69–74. doi:10.1016/j.intermet.2015.07.018.

[21] X. Wang, S. Kustov, K. Li, D. Schryvers, B. Verlinden, J. Van Humbeeck, Effect of nanoprecipitates on the transformation behavior and functional properties of a Ti-50.8 at.% Ni alloy with micron-sized grains, Acta Mater. 82 (2015) 224–233. doi:10.1016/j.actamat.2014.09.018.

[22] R. Plietsch, K. Ehrlich, Strength differential effect in psuedoelastic NiTi shape memory alloys, Acta Metall. 45 (1997) 2417–2424. doi:http://dx.doi.org/10.1016/S1359-6454(96)00354-0.

[23] R.F. Zhu, J.N. Liu, G.Y. Tang, S.Q. Shi, M.W. Fu, Z.T.H. Tse, The improved superelasticity of NiTi alloy via electropulsing treatment for minutes, J. Alloys Compd. 584 (2014) 225–231. doi:10.1016/j.jallcom.2013.09.040.

[24] D. Favier, Y. Liu, L. Orgéas, a. Sandel, L. Debove, P. Comte-Gaz, Influence of thermomechanical processing on the superelastic properties of a Ni-rich Nitinol shape memory alloy, Mater. Sci. Eng. A. 429 (2006) 130–136. doi:10.1016/j.msea.2006.05.018.

[25] A. Saigal, M. Fonte, Solid, shape recovered “bulk” Nitinol: Part I-Tension-compression asymmetry, Mater. Sci. Eng. A. 528 (2011) 5536–5550. doi:10.1016/j.msea.2011.03.060.

[26] Y. Liu, Z. Xie, J. Van Humbeeck, L. Delaey, Asymmetry of stress–strain curves under tension and compression for NiTi shape memory alloys, Acta Mater. 46 (1998) 4325–4338. doi:10.1016/S1359-6454(98)00112-8.

[27] V. Grolleau, H. Louche, V. Delobelle, a. Penin, G. Rio, Y. Liu, D. Favier, Assessment of tension-compression asymmetry of NiTi using circular bulge testing of thin plates, Scr. Mater. 65 (2011) 347–350. doi:10.1016/j.scriptamat.2011.05.003.

[28] C. Grabe, O.T. Bruhns, On the viscous and strain rate dependent behavior of polycrystalline NiTi, Int. J. Solids Struct. 45 (2008) 1876–1895. doi:10.1016/j.ijsolstr.2007.10.029.

[29] C. Elibol, M.F.X. Wagner, Strain rate effects on the localization of the stress-induced martensitic transformation in pseudoelastic NiTi under uniaxial tension, compression and compression-shear, Mater. Sci. Eng. A. 643 (2015) 194–202. doi:10.1016/j.msea.2015.07.039.

[30] K. Gall, H. Sehitoglu, Y.I. Chumlyakov, I. V. Kireeva, Tension-compression asymmetry of the stress-strain response in aged single crystal and polycrystalline NiTi, Acta Mater. 47 (1999) 1203–1217. doi:10.1016/S1359-6454(98)00432-7.

[31] M.R.K. Ravari, M. Kadkhodaei, a Ghaei, A microplane constitutive model for shape memory alloys considering tension–compression asymmetry, Smart Mater. Struct. 24 (2015) 075016. doi:10.1088/0964-1726/24/7/075016.

[32] Y.F. Wang, Z.F. Yue, J. Wang, The effect of grain orientation on the tensile-compressive asymmetry of polycrystalline NiTi shape memory alloy, Materwiss. Werksttech. 38 (2007) 2–6. doi:10.1002/mawe.200700136.

[33] R. Mirzaeifar, R. Desroches, A. Yavari, K. Gall, A micromechanical analysis of the coupled thermomechanical superelastic response of textured and untextured polycrystalline NiTi shape memory alloys, Acta Mater. 61 (2013) 4542–4558. doi:10.1016/j.actamat.2013.04.023.

[34] B. Reedlunn, C.B. Churchill, E.E. Nelson, J.A. Shaw, S.H. Daly, Tension, compression, and bending of superelastic shape memory alloy tubes, J. Mech. Phys. Solids. 63 (2014) 506–537. doi:10.1016/j.jmps.2012.12.012.

[35] P. Sittner, V. Novak, Anisotropy of martensitic transformations in modeling of shape memory alloy polycrystals, Int. J. Plast. 16 (2000) 1243–1268.

[36] A.P. Stebner, S.C. Vogel, R.D. Noebe, T. a. Sisneros, B. Clausen, D.W. Brown, A. Garg, L.C. Brinson, Micromechanical quantification of elastic, twinning, and slip strain partitioning exhibited by polycrystalline, monoclinic nickel-titanium during large uniaxial

deformations measured via in-situ neutron diffraction, J. Mech. Phys. Solids. 61 (2013) 2302–2330. doi:10.1016/j.jmps.2013.05.008.

[37] A.N. Bucsek, H.M. Paranjape, A.P. Stebner, Myths and Truths of Nitinol Mechanics: Elasticity and Tension–Compression Asymmetry, Shape Mem. Superelasticity. 2 (2016) 264–271. doi:10.1007/s40830-016-0074-z.

[38] S.C. Mao, X.D. Han, Y.B. Tian, J.F. Luo, Z. Zhang, Y. Ji, M.H. Wu, In situ EBSD investigations of the asymmetric stress-induced martensitic transformation in TiNi shape memory alloys under bending, Mater. Sci. Eng. A. 498 (2008) 278–282. doi:10.1016/j.msea.2008.07.072.

[39] S.C. Mao, J.F. Luo, Z. Zhang, M.H. Wu, Y. Liu, X.D. Han, EBSD studies of the stress-induced B2-B19′ martensitic transformation in NiTi tubes under uniaxial tension and compression, Acta Mater. 58 (2010) 3357–3366. doi:10.1016/j.actamat.2010.02.009.

[40] K. Kazemi-Choobi, J. Khalil-Allafi, V. Abbasi-Chianeh, Influence of recrystallization and subsequent aging treatment on superelastic behavior and martensitic transformation of Ni50.9Ti wires, J. Alloys Compd. 582 (2014) 348–354. doi:10.1016/j.jallcom.2013.08.063.

[41] K. Kazemi-Choobi, J. Khalil-Allafi, V. Abbasi-Chianeh, Investigation of the recovery and recrystallization processes of Ni 50.9Ti49.1 shape memory wires using in situ electrical resistance measurement, Mater. Sci. Eng. A. 551 (2012) 122–127. doi:10.1016/j.msea.2012.04.106.

[42] ASTM-E9, Standard test methods of compression testing of metallic materials at room temperature, West Conshohocken, PA ASTM Int. (2000) 98–105.

[43] ASTM-E8, Standard test method for tension testing of metallic materials, West Conshohocken ASTM Int. (2004).

[44] H. Sehitoglu, I. Karaman, R. Anderson, X. Zhang, K. Gall, H.J. Maier, Y. Chumlyakov, Compressive response of NiTi single crystals, Acta Mater. 48 (2000) 3311–3326. doi:10.1016/S1359-6454(00)00153-1.

[45] S. Miyazaki, K. Otsuka, Y. Suzuki, Transformation pseudoelasticity and deformation

behavior in a Ti-50.6at%Ni alloy, Scr. Metall. 15 (1981) 287–292. doi:10.1016/0036-9748(81)90346-X.

[46] O. Molnárová, P. Šittner, J. Veselý, M. Cieslar, TEM analysis of deformation bands created by tensile deformation of superelastic NiTi wires, Mater. Charact. 167 (2020). doi:10.1016/j.matchar.2020.110470.

[47] X.B. Wang, B. Verlinden, J. Van Humbeeck, R-phase transformation in NiTi alloys, Mater. Sci. Technol. 000 (2014) 1743284714Y.0000000590. doi:10.1179/1743284714Y.0000000590.

[48] T.W. Duerig, K. Bhattacharya, The Influence of the R-Phase on the Superelastic Behavior of NiTi, Shape Mem. Superelasticity. 1 (2015) 153–161. doi:10.1007/s40830-015-0013-4.

[49] L. Hu, S. Jiang, S. Liu, Y. Zhang, Y. Zhao, C. Zhao, Transformation twinning and deformation twinning of NiTi shape memory alloy, Mater. Sci. Eng. A. 660 (2016) 1–10. doi:10.1016/j.msea.2016.02.066.

[50] M.E. Mitwally, M. Farag, Effect of cold work and annealing on the structure and characteristics of NiTi alloy, Mater. Sci. Eng. A. 519 (2009) 155–166. doi:10.1016/j.msea.2009.04.057.

[51] A.S. Mahmud, H. Yang, S. Tee, G. Rio, Y. Liu, Effect of annealing on deformation-induced martensite stabilisation of NiTi, Intermetallics. 16 (2008) 209–214. doi:10.1016/j.intermet.2007.09.003.

[52] X. Yan, J. Van Humbeeck, Effect of annealing on martensite stabilization due to deformation via cooling under stress in cold-worked NiTi thin wire, Mater. Sci. Eng. A. 558 (2012) 737–741. doi:10.1016/j.msea.2012.08.090.

[53] H. Shahmir, M. Nili-Ahmadabadi, A. Razzaghi, M. Mohammadi, C.T. Wang, J.M. Jung, H.S. Kim, T.G. Langdon, Using dilatometry to study martensitic stabilization and recrystallization kinetics in a severely deformed NiTi alloy, J. Mater. Sci. 50 (2015) 4003–4011. doi:10.1007/s10853-015-8957-5.

[54] J. Burow, E. Prokofiev, C. Somsen, J. Frenzel, R.Z. Valiev, G.F. Eggeler, Martensitic Transformations and Functional Stability in Ultra-Fine Grained NiTi Shape Memory

Alloys, Mater. Sci. Forum. 584–586 (2008) 852–857. doi:10.4028/www.scientific.net/MSF.584-586.852.

[55] a. S. Paula, J.P.H.G. Canejo, N. Schell, F.M.B. Fernandes, Structural evolution on thermal cycling in Ti-rich NiTi SMA, Nucl. Instruments Methods Phys. Res. Sect. B Beam Interact. with Mater. Atoms. 238 (2005) 111–114. doi:10.1016/j.nimb.2005.06.028.

[56] M. Karimzadeh, M.R. Aboutalebi, M.T. Salehi, S.M. Abbasi, M. Morakabati, Effects of thermomechanical treatments on the martensitic transformation and critical stress of Ti–50.2at.% Ni alloy, J. Alloys Compd. 637 (2015) 171–177. doi:10.1016/j.jallcom.2015.02.195.

[57] A. Ahadi, Q. Sun, Effects of grain size on the rate-dependent thermomechanical responses of nanostructured superelastic NiTi, Acta Mater. 76 (2014) 186–197. doi:10.1016/j.actamat.2014.05.007.

[58] E. Polatidis, M. Šmíd, I. Kuběna, W.N. Hsu, G. Laplanche, H. Van Swygenhoven, Deformation mechanisms in a superelastic NiTi alloy: An in-situ high resolution digital image correlation study, Mater. Des. 191 (2020) 1–10. doi:10.1016/j.matdes.2020.108622.

[59] X. Kong, Y. Yang, Z. Sun, H. Yang, Y. Liu, Y. Ren, L. Cui, C. Chen, S. Hao, In-situ high energy X-ray diffraction study of microscopic deformation behavior of martensite variant reorientation in NiTi wire, Appl. Mater. Today. 22 (2021) 100904. doi:10.1016/j.apmt.2020.100904.

[60] H. Zhang, X. Li, X. Zhang, Grain-size-dependent martensitic transformation in bulk nanocrystalline TiNi under tensile deformation, J. Alloys Compd. 544 (2012) 19–23. doi:10.1016/j.jallcom.2012.08.014.

Figures

Fig. 1. The schematic representation of the asymmetric behavior of an NiTi alloy during tensile and compressive modes of deformation. The most important asymmetry parameters are identified in the figure.

Fig. 2. (a) X-ray diffraction pattern, and (b) the grain size distribution of the solution annealed (SA) specimen.

Fig. 3. (a) acquired curves from tension and compression load-unload cyclic test for solution annealed (SA) specimen and (b) the measured superelasticity parameters.

Fig. 4. Superelasticity load-unload curves in each mode of deformation and the measured parameters for (a,c) CC-0.2-400-120 and (b,d) CC-0.5-400-60.

Fig. 5. (a) Inverse pole figure (IPF) of the B2 austenite phase, representing the initial texture and (b) misorientation angle frequency of the solution annealed specimen.

Fig. 6. Inverse pole figures (IPFs), representing the texture of the material for (a) CC-0.2-400-120 and (b) CC-0.5-400-60.

Fig. 7. TEM images and SAED patterns of CC-0.2-400-120, revealing (left column) bright field images of different areas of the sample, (middle column) the higher magnification bright field images of the same area (middle), in which the dashed circle signifies the regions for SAED pattern acquisition, and (right) the corresponding indexed SAED patterns. (a-c) reveals the existence of austenite bands and the presence of B2 phase in the SAED pattern, (d-f) displays the lenticular Ni4Ti3 precipitates and the formation of R-phase in their vicinity according to the SAED pattern, and (g-i) indicates the presence of martensite twins, which were indexed as compound twins in the SAED pattern.

Fig. 8. TEM images and SAED patterns of CC-0.5-400-60, revealing (left column) bright field images of different areas of the sample, (middle column) the higher magnification bright field images of the same area (middle), in which the dashed circle signifies the regions for SAED pattern acquisition, and (right) the corresponding indexed SAED patterns. (a-c) reveals the presence of a very refined grain structure, which were indexed as B2 austenite phase, and (d-f) depicts the presence of martensite twins in the structure, which were indexed to be (001) compound twins in the SAED pattern, formed during the cold working process to true strain of 0.5

Fig. 9. Misorientation angle distribution for CC-0.2-400-120 and CC-0.5-400-60 samples, showing low angle and high angle grain boundaries.

Fig. 10. EBSD inverse pole figures along the loading direction of superelastic tension or compression test for (a) SA, (b) CC-0.2-400-120 and (c) CC-0.5-400-60, showing the orientation of each scanned spot on the sample.

Fig. 11. (a) Schmid factor and (b) transformation strain calculation with respect to different loading direction for tensile and compressive mode of deformation, acquired from Mao et. al [39].

Fig. 12. Superimposition of spot orientation distribution on Schmid factor and transformation strain calculation, in a unique inverse pole figure.

Tables

Table 1. Summary of the implemented cold working and subsequent annealing conditions and the measured values of SIM stress and residual strain measured from load-unload tensile testing. More detailed information is presented in [14].

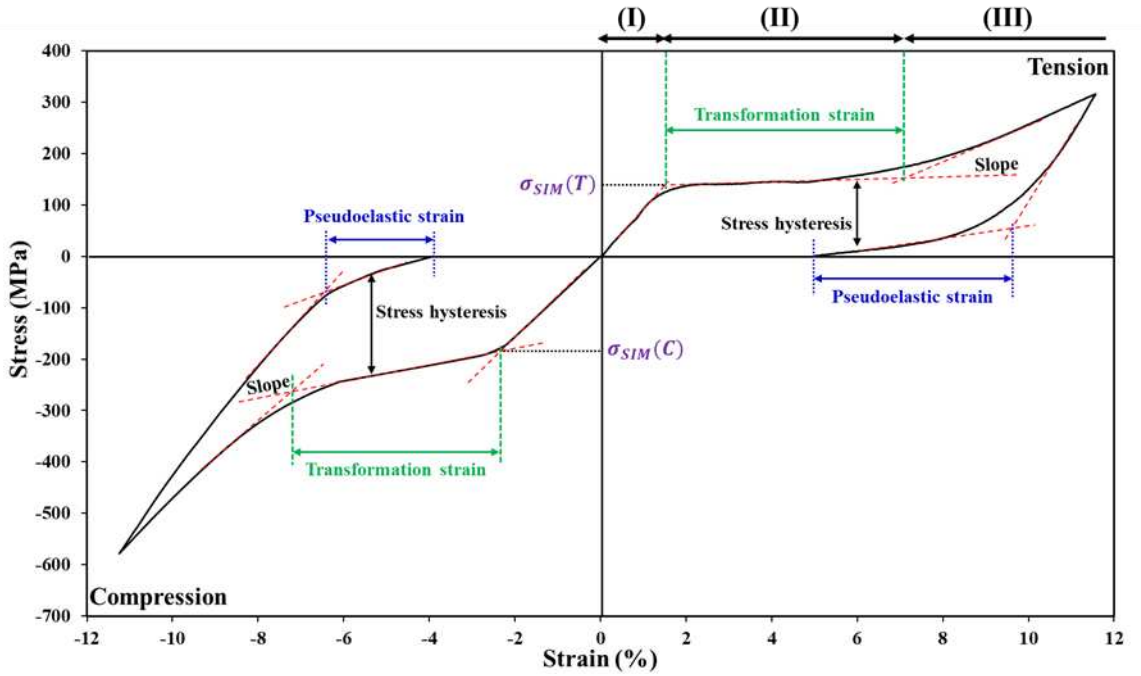

Fig. 1. The schematic representation of the asymmetric behavior of an NiTi alloy during tensile and compressive modes of deformation. The most important asymmetry parameters are identified in the figure.

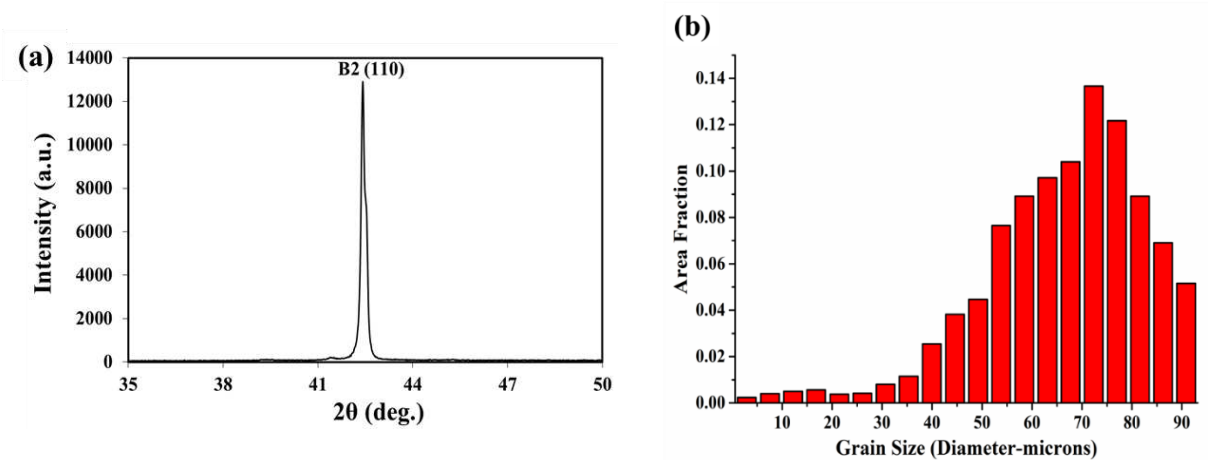

Fig. 2. (a) X-ray diffraction pattern, and (b) the grain size distribution of the solution annealed (SA) specimen.

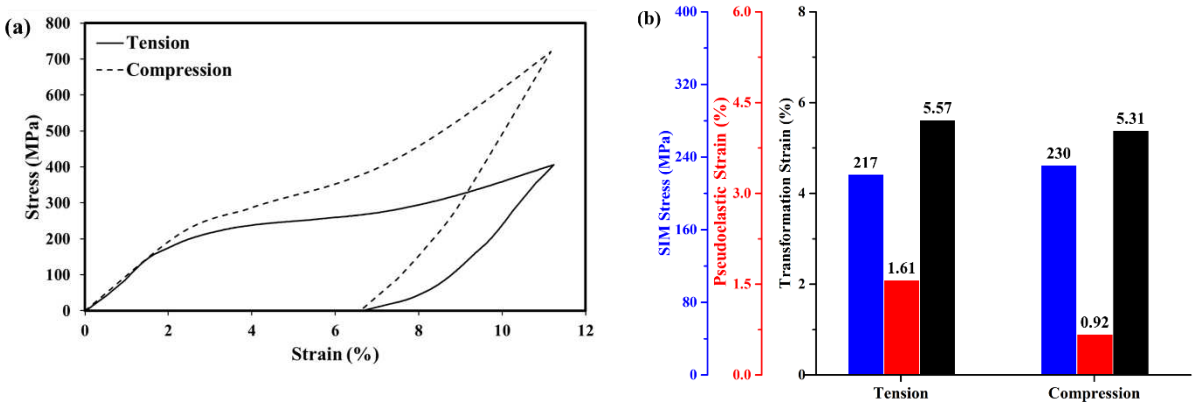

Fig. 3. (a) acquired curves from tension and compression load-unload cyclic test for solution annealed (SA) specimen and (b) the measured superelasticity parameters.

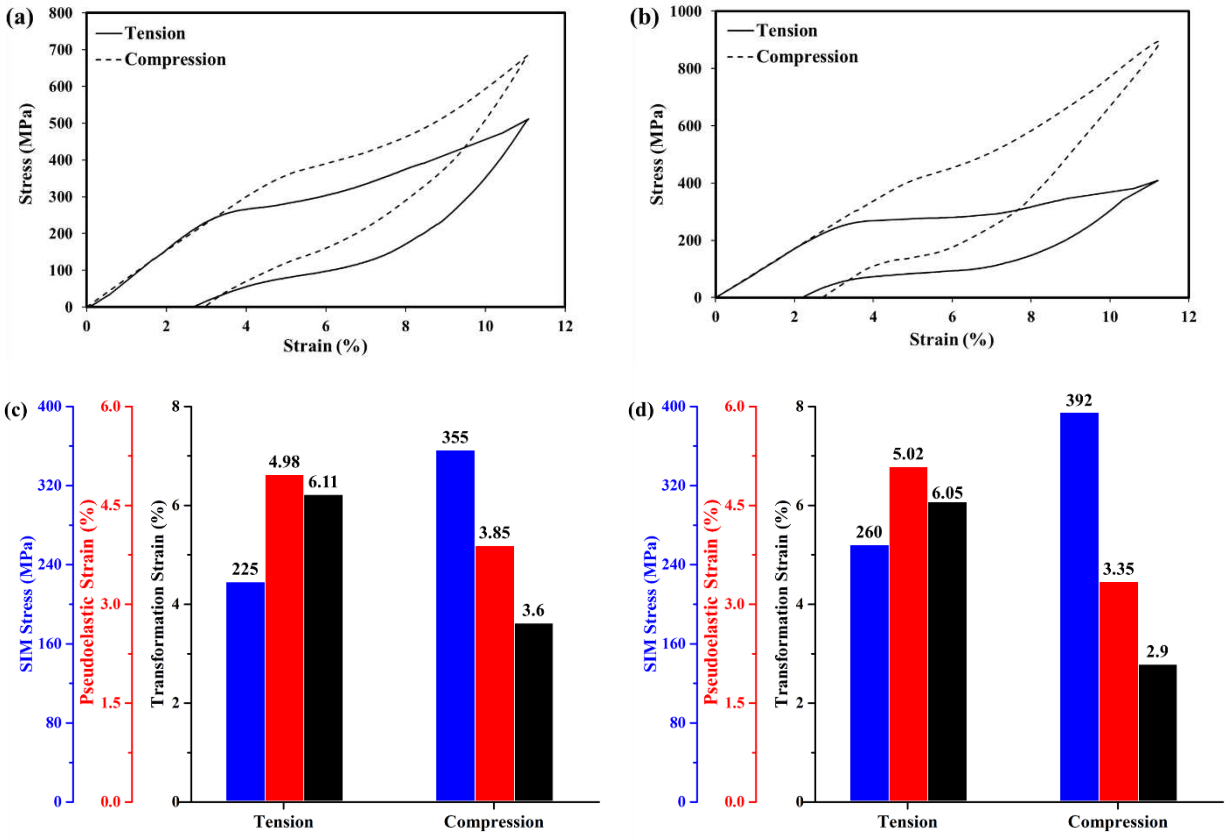

Fig. 4. Superelasticity load-unload curves in each mode of deformation and the measured parameters for (a,c) CC-0.2-400-120 and (b,d) CC-0.5-400-60.

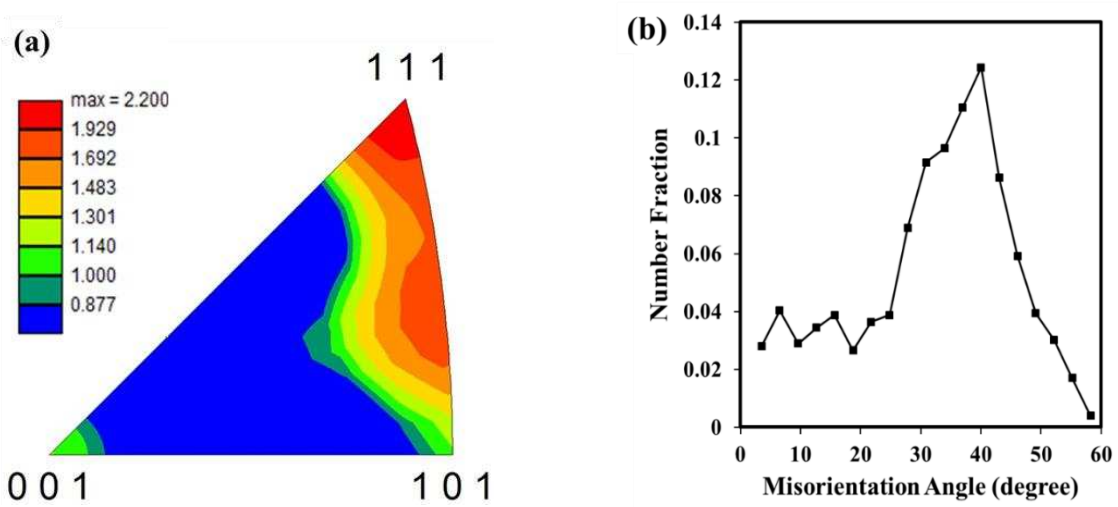

Fig. 5. (a) Inverse pole figure (IPF) of the B2 austenite phase, representing the initial texture and (b) misorientation angle frequency of the solution annealed specimen.

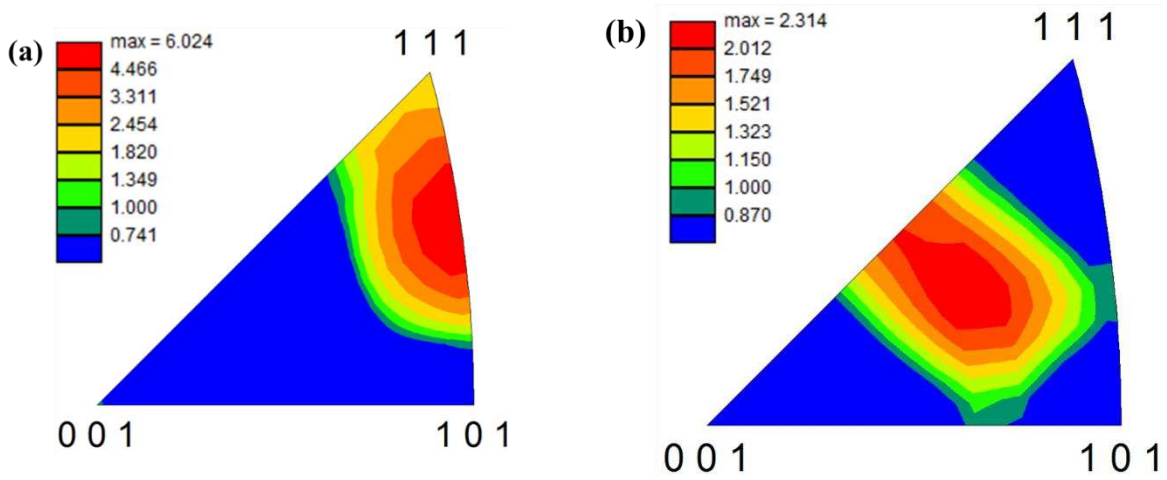

Fig. 6. Inverse pole figures (IPFs), representing the texture of the material for (a) CC-0.2-400-120 and (b) CC-0.5-400-60.

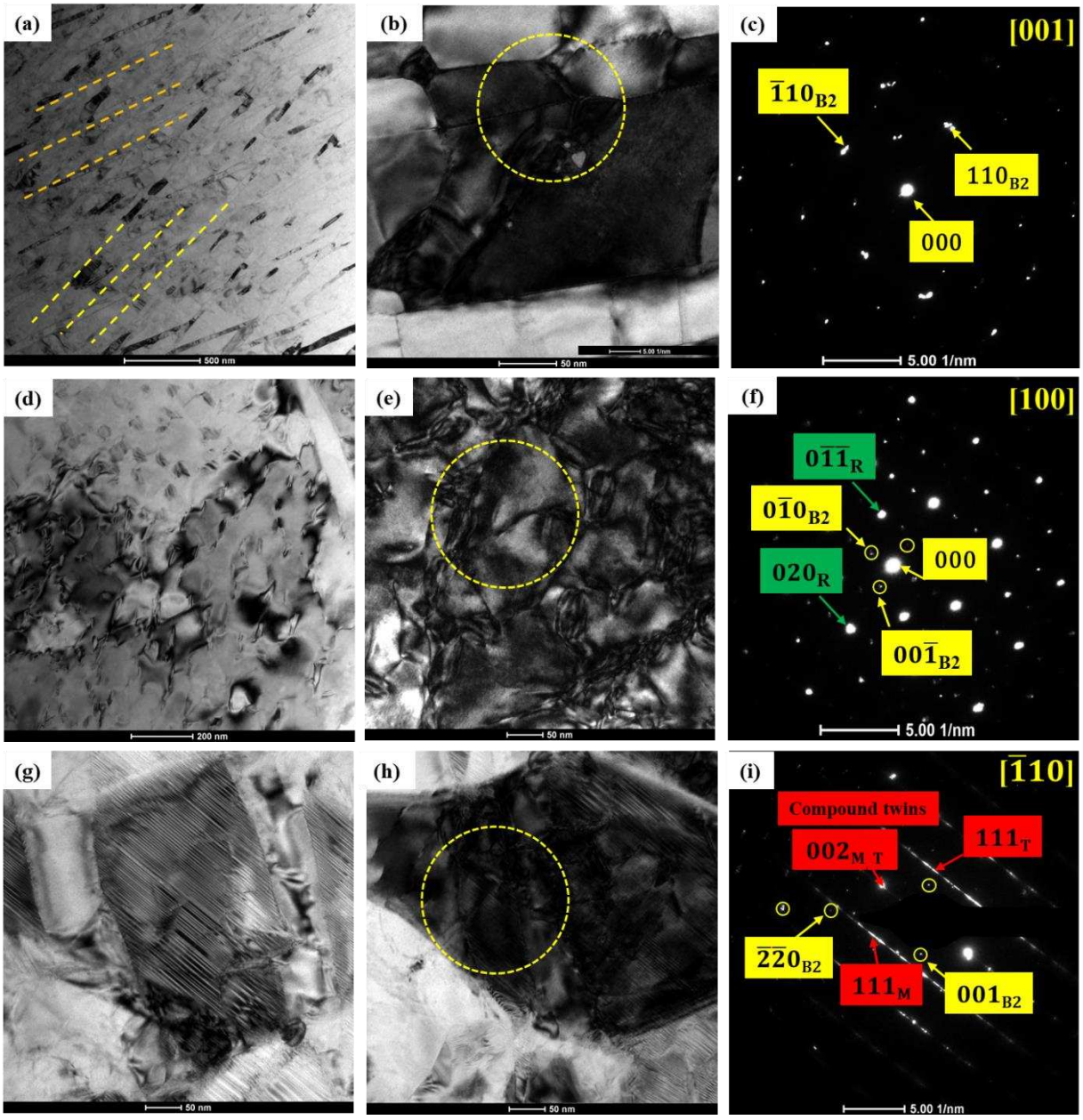

Fig. 7. TEM images and SAED patterns of CC-0.2-400-120, revealing (left column) bright field images of different areas of the sample, (middle column) the higher magnification bright field images of the same area (middle), in which the dashed circle signifies the regions for SAED pattern acquisition, and (right) the corresponding indexed SAED patterns. (a-c) reveals the existence of austenite bands and the presence of B2 phase in the SAED pattern, (d-f) displays the lenticular Ni_4Ti_3 precipitates and the formation of R-phase in their vicinity according to the SAED pattern, and (g-i) indicates the presence of martensite twins, which were indexed as (001) martensite compound twins in the SAED pattern.

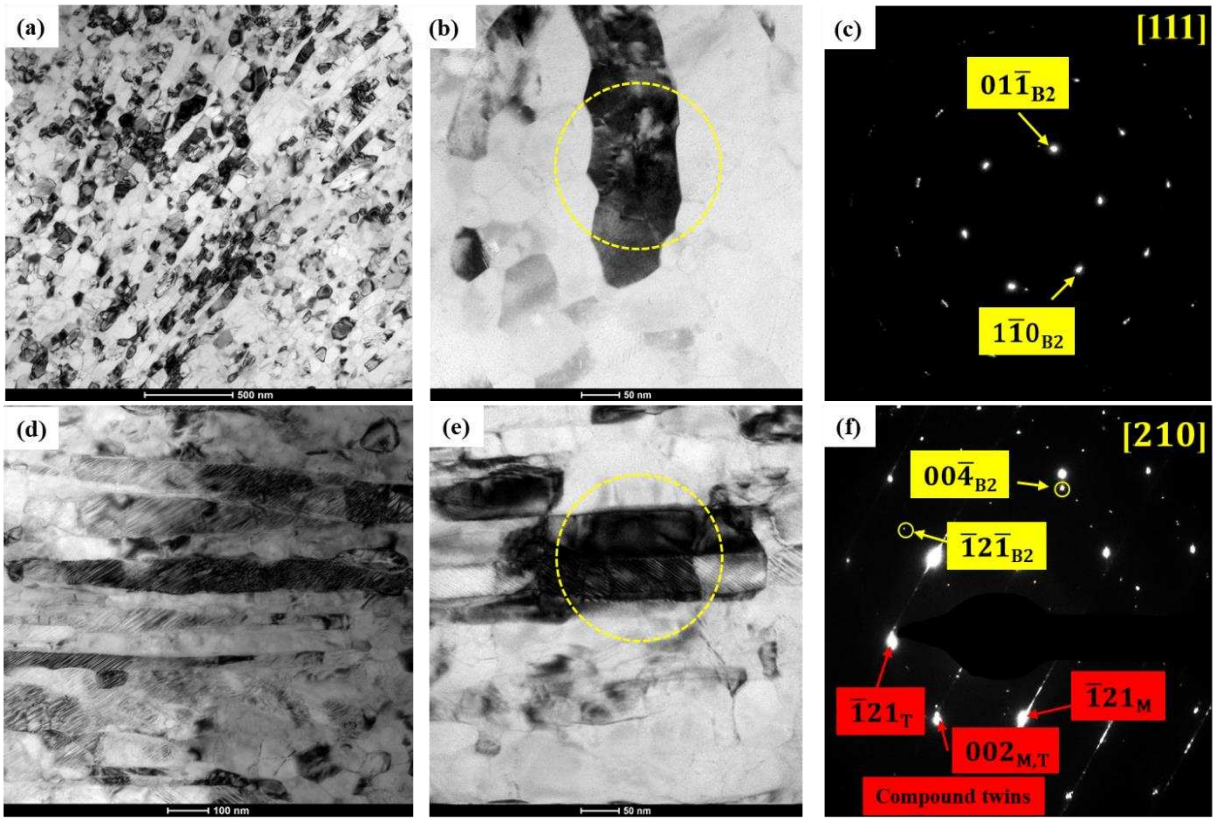

Fig. 8. TEM images and SAED patterns of CC-0.5-400-60, revealing (left column) bright field images of different areas of the sample, (middle column) the higher magnification bright field images of the same area (middle), in which the dashed circle signifies the regions for SAED pattern acquisition, and (right) the corresponding indexed SAED patterns. (a-c) reveals the presence of a very refined grain structure, which were indexed as B2 austenite phase, and (d-f) depicts the presence of martensite twins in the structure, which were indexed to be (001) compound twins in the SAED pattern, formed during the cold working process to true strain of 0.5

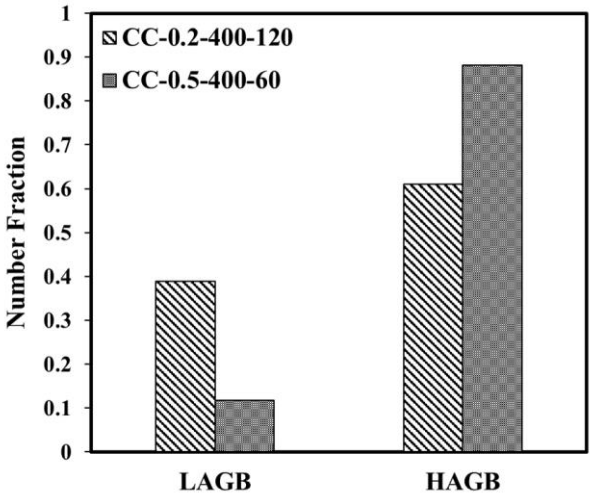

Fig. 9. Misorientation angle distribution for CC-0.2-400-120 and CC-0.5-400-60 samples, showing low angle and high angle grain boundaries.

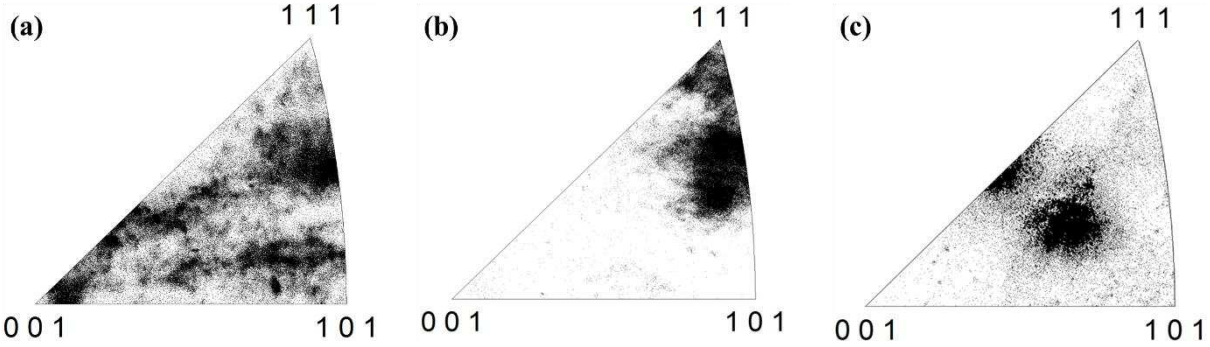

Fig. 10. EBSD inverse pole figures along the loading direction of superelastic tension or compression test for (a) SA, (b) CC-0.2-400-120 and (c) CC-0.5-400-60, showing the orientation of each scanned spot on the sample.

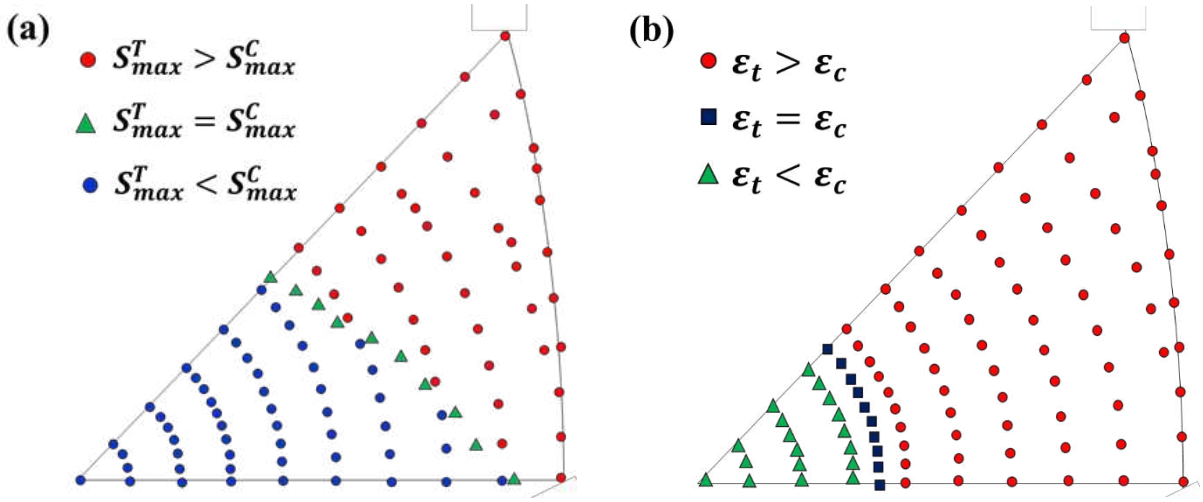

Fig. 11. (a) Schmid factor and (b) transformation strain calculation with respect to different loading direction for tensile and compressive mode of deformation, acquired from Mao et. al [39].

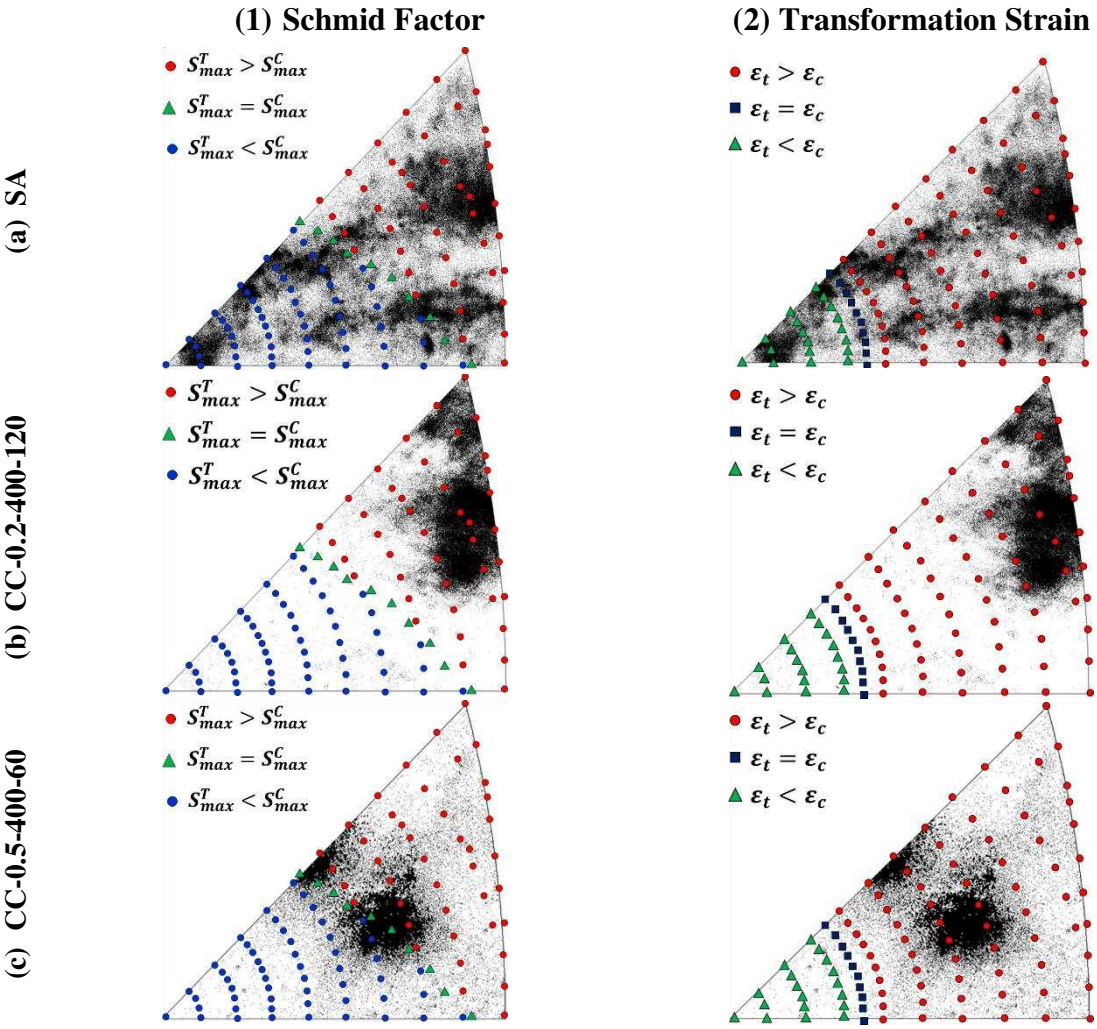

Fig. 12. Superimposition of spot orientation distribution on Schmid factor and transformation strain calculation, in a unique inverse pole figure.

Table 1. Summary of the implemented cold working and subsequent annealing conditions and the measured values of SIM stress and residual strain measured from load-unload tensile testing. More detailed information is presented in [14].

Sample Name	Cold working and annealing conditions			Results of loading to 11% engineering strain and unloading	
	True strain	Temperature (°C)	Time (min)	SIM stress (MPa)	Residual strain (%)
CC-0.2-400-10	0.2	400	10	181	7
CC-0.2-400-30			30	173	7.4
CC-0.2-400-60			60	224	6.1
CC-0.2-400-120			120	225	2.6
CC-0.2-500-10		500	10	192	7.2
CC-0.2-500-30			30	83	7.9
CC-0.2-500-60			60	241	4.1
CC-0.2-500-120			120	162	7.2
CC-0.5-400-10	0.5	400	10	323	-
CC-0.5-400-30			30	186	-
CC-0.5-400-60			60	263	2.1
CC-0.5-400-120			120	178	4.3
CC-0.5-500-10		500	10	252	2.7
CC-0.5-500-30			30	225	3.8
CC-0.5-500-60			60	202	4.1
CC-0.5-500-120			120	103	8.3